iScience

CellPress
OPEN ACCESS

Article

Mitochondrial Protrusions in Neuronal Cells

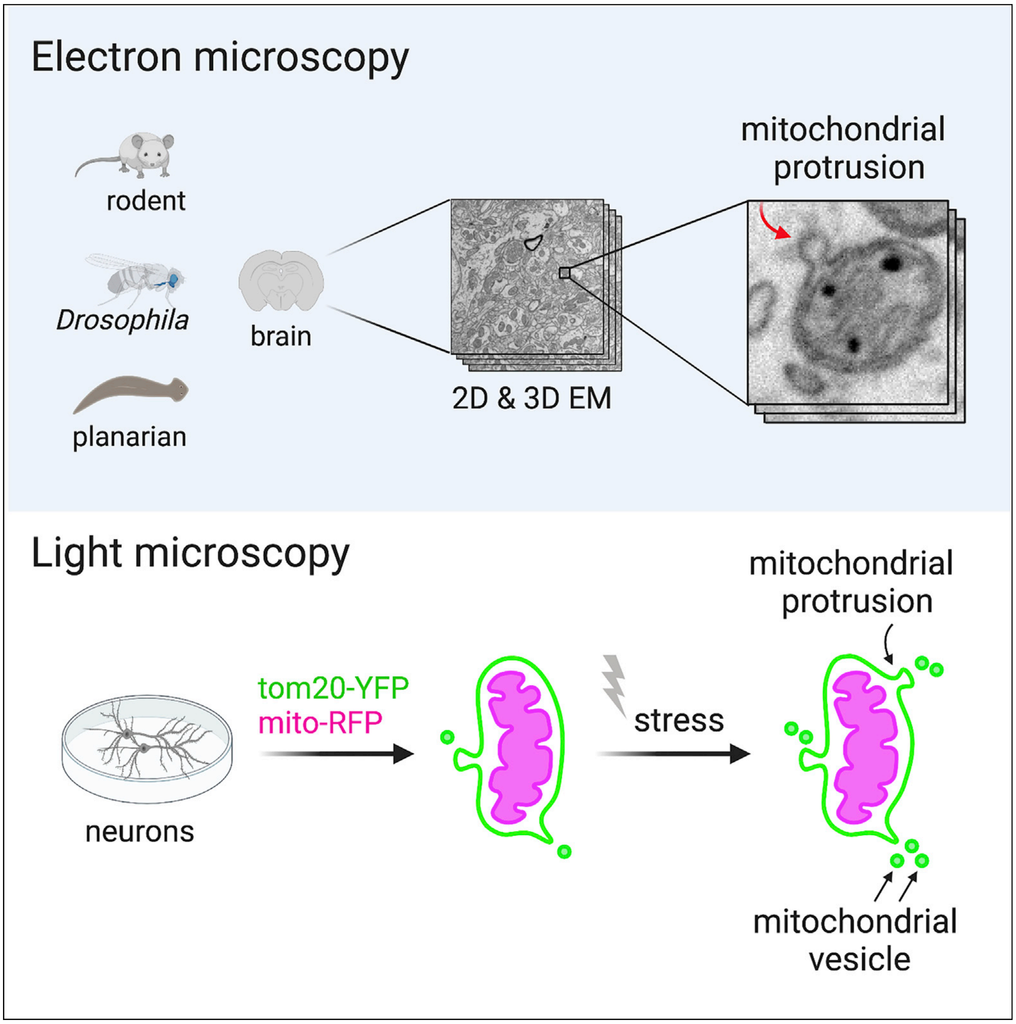

Pamela J. Yao, Erden Eren, Ronald S. Petralia, Jeffrey W. Gu, Ya-Xian Wang, Dimitrios Kapogiannis

pamela.yao@nih.gov (P.J.Y.)
kapogiannisd@mail.nih.gov (D.K.)

HIGHLIGHTS

2D and 3D EM visualizes mitochondrial protrusions in the brain

Rodent, *Drosophila*, and planarian neurons display similar ultrastructure of protrusions

Light microscopy of mitochondrial markers shows mitochondrial protrusions and vesicles

Neurons under mild stress produce more mitochondrial protrusions and vesicles

Yao et al., iScience *23*, 101514
September 25, 2020
https://doi.org/10.1016/j.isci.2020.101514

iScience

CellPress OPEN ACCESS

Article

Mitochondrial Protrusions in Neuronal Cells

Pamela J. Yao,[1,4,*] Erden Eren,[1,3] Ronald S. Petralia,[2,3] Jeffrey W. Gu,[1] Ya-Xian Wang,[2] and Dimitrios Kapogiannis[1,*]

SUMMARY

Mitochondrial function relies on multiple quality control mechanisms, including the release of mitochondrial vesicles. To investigate the ultrastructure and prevalence of mitochondrial membranous protrusions (and, by extension, vesicles) in neurons, we surveyed mitochondria in rat and planarian brains using transmission electron microscopy (EM). We observed that mitochondrial protrusions mostly extend from the outer membrane. Leveraging available 3D EM datasets of the brain, we further analyzed mitochondrial protrusions in neurons of mouse and *Drosophila* brains, identifying high-resolution spatial views of these protrusions. To assess whether the abundance of mitochondrial protrusions and mitochondria-derived vesicles respond to cellular stress, we examined neurons expressing fluorescently tagged mitochondrial markers using confocal microscopy with Airyscan and found increased numbers of mitochondrial protrusions and vesicles with mild stress. Future studies using improved spatial resolution with added temporal information may further define the functional implications of mitochondrial protrusions and vesicles in neurons.

INTRODUCTION

A well-studied quality control mechanism for mitochondria is mitophagy, a specialized form of autophagy in which unhealthy mitochondria are surrounded by autophagosomes and subsequently broken up by lysosomes (Gatica et al., 2018; Parzych and Klionsky, 2014; Pickles et al., 2018). In addition to mitophagy, burgeoning evidence suggests that vesicles that bud from mitochondria, dubbed mitochondria-derived vesicles (Cadete et al., 2016; McLelland et al., 2014; Roberts et al., 2016; Sugiura et al., 2014; Yamashita et al., 2016), are another mechanism for cells to maintain healthy mitochondria (Misgeld and Schwarz, 2017; Youle, 2019). These small mitochondrial vesicles (50–150 nm) often carry oxidized proteins (Soubannier et al., 2012b; Sugiura et al., 2014). Although the specific proteins being carried by these vesicles vary depending on the types of cellular stress (Soubannier et al., 2012a, 2012b; Sugiura et al., 2014), the vesicles mostly end up merging with lysosomes (Soubannier et al., 2012a; McLelland et al., 2014) or peroxisomes (Braschi et al., 2010; Neuspiel et al., 2008), suggesting that their primary role is to remove and dispose of damaged mitochondrial proteins or small parts of the organelle. Because the cellular stresses that elicit the production of the mitochondrial vesicles are in general milder than the stresses that trigger mitophagy, it is believed that the mitochondrial vesicles provide a constant or early-step quality control mechanism for the mitochondria prior to mitophagy (Cadete et al., 2016; Misgeld and Schwarz, 2017; Picca et al., 2020; Youle, 2019).

There is also evidence that the mitochondrial vesicles have other roles besides disposal of mitochondrial bits. In immune cells, the mitochondrial vesicles are directly involved in presenting mitochondrial antigens to the plasma membrane (Matheoud et al., 2016). In bacteria-infected macrophages, mitochondrial vesicles facilitate destroying pathogens by supplying the phagosomes with H_2O_2 (Abuaita et al., 2018). In neurons, where the mitochondria must adapt to an intricate cellular architecture and meet high energy demands (Ashrafi et al., 2020; Harris et al., 2012; Misgeld and Schwarz, 2017; Rangaraju et al., 2019), mitochondrial vesicles carry out specialized functions. For example, in neurons under mild stress or in neurons involved in certain chronic pathological conditions, the mitochondrial vesicles liberate the mitochondrion-anchoring protein Syntaphilin from mitochondria, thus allowing the stressed mitochondria to traffic to the cell body for repair before activation of mitophagy (Lin et al., 2017). Notably, Syntaphilin exists only in axonal mitochondria (Kang et al., 2008; Lin et al., 2017); therefore, the vesicle-mediated Syntaphilin release may serve as a specific mechanism for maintaining and renewing mitochondria that reside in long and extended axons.

[1] Laboratory of Clinical Investigation, NIA/NIH Biomedical Research Center, Baltimore, MD 21224, USA

[2] Advanced Imaging Core, NIDCD/NIH, Bethesda, MD 20892, USA

[3] These authors contributed equally

[4] Lead Contact

*Correspondence: pamela.yao@nih.gov (P.J.Y.), kapogiannisd@mail.nih.gov (D.K.)

https://doi.org/10.1016/j.isci.2020.101514

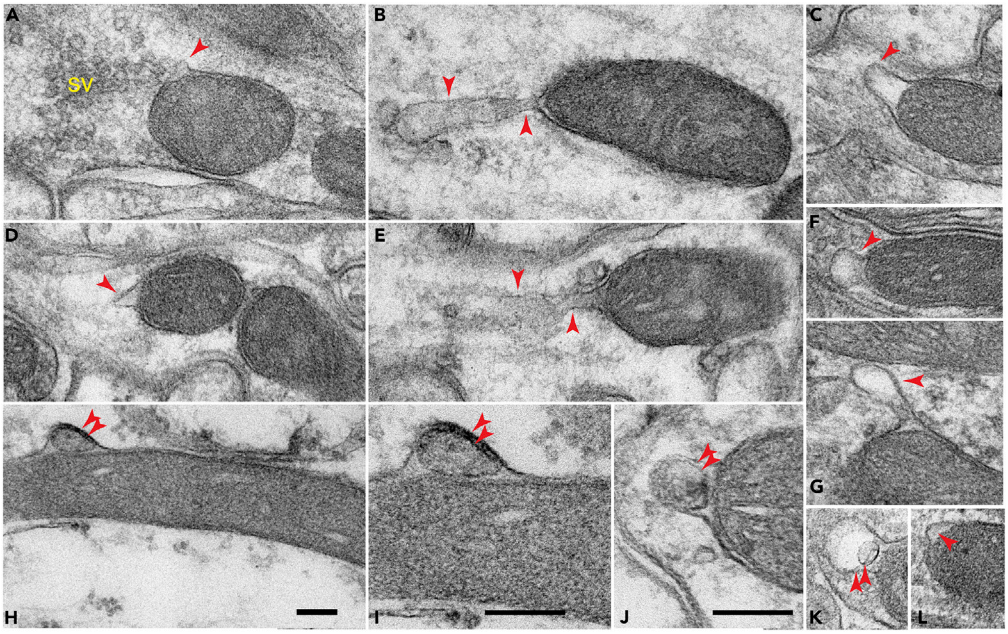

Figure 1. Electron Microscopic Examination of the CA1 Stratum Radiatum/Pyramidale Area of the Rat Hippocampus Reveals the Ultrastructure of Mitochondrial Protrusions

(A–G, and L) Some of the protrusions are relatively small (~100 nm) with either wide or narrow necks (arrowheads in A, C, D, F, and G), whereas others are long tubulovesicular structures extending from the mitochondria (arrowheads in B and E). Typically, these protrusions are derived from the outer mitochondrial membrane; only some of them also include the inner mitochondrial membranes (double arrowheads in H–K). I is an enlarged view of (H). Scale bars in (H)–(J), 100 nm; scale bar in (H) applies to all other micrographs. Note: (A), (F), axonal terminals; (B), (E), and (J), large or small dendrites; (C), (D), (K), and (L), neurites of unclear identity; (H) and (I), glial process. sv, synaptic vesicle clusters. A total of three rats were examined.

In principle, mitochondrial vesicles in different parts of the neuron or in different types of neurons and other brain cells could have diverse specialized roles in sustaining healthy and competent mitochondria; therefore, there is a need for a comprehensive understanding of mitochondrial vesicles in brain cells. In this study, we examined and characterized mitochondrial membranous protrusions and vesicles in the rodent, planarian, and *Drosophila* brains using electron microscopy (EM) and in cultured neurons using light microscopy.

RESULTS

Mitochondrial Protrusions in Brain Cells

We first surveyed the rat brain using conventional transmission electron microscopy (TEM). Focusing on neurons in the CA1 stratum radiatum/pyramidale area of the hippocampus, we readily observed membranous protrusions on mitochondria (Figure 1). In general, these mitochondrial protrusions were small, with a diameter of 50–150 nm; some of them had pointed tops and wide bases (i.e., Figures 1A, 1D, and 1L), whereas others had rounded tops and tapered bases (i.e., Figures 1F and 1G). In a few cases, the protrusions were relatively large with elongated necks extending from the mitochondria (Figures 1B and 1E). Regardless of the size and shape, most of the mitochondrial protrusions contained a single membrane—a continuation of the outer membrane of the parent mitochondria (arrowheads); on rare occasions, we observed mitochondrial protrusions including both the outer and inner mitochondrial membranes (double arrowheads; Figures 1H–1K).

To evaluate whether these findings could extend to other species, we examined the brain of the planarian flatworm, the simplest animals with a definitive brain (Petralia et al., 2015, 2016). In the planarian brain, we found examples of protrusions on mitochondria located in synapses or synaptic vesicle-filled axonal terminals and in various processes interspersed in the neuropil (Figure 2). Overall, the size and morphology of the mitochondrial protrusions in the planarian brain were similar to those in the rat brain. For example, the

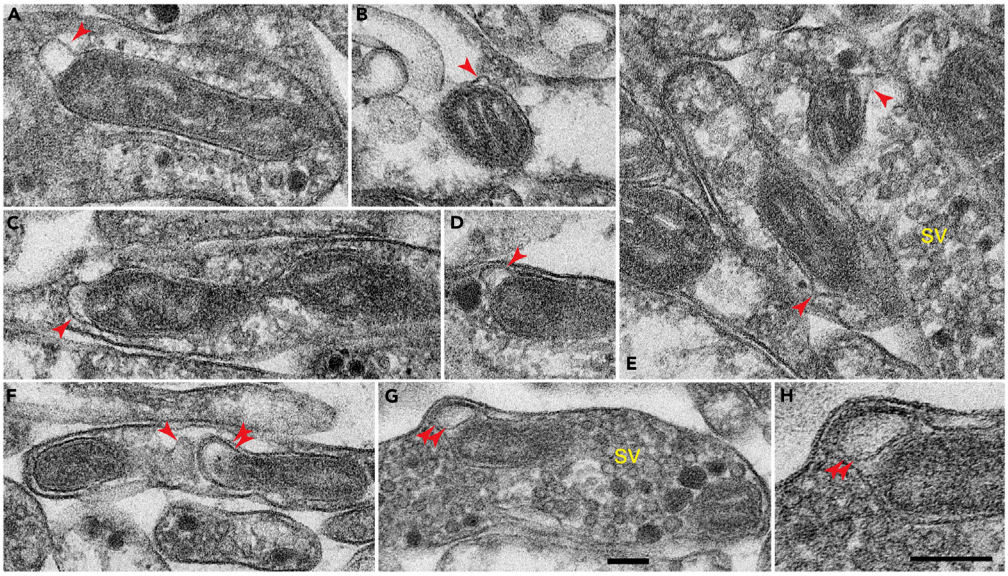

Figure 2. Electron Microscopic Examples of Mitochondrial Protrusions in the Brain of the Planaria

As in the rat brain, most of the mitochondrial protrusions (arrowheads) are derived from the outer mitochondrial membrane; few of them also include the inner mitochondrial membranes (double arrowheads in F–H). (H) is an enlarged view of (G). Scale bars in (G) and (H), 100 nm; scale bar in (G) applies to all other micrographs. sv, synaptic vesicle clusters. Two planaria were examined.

planarian mitochondrial protrusions shown in Figure 2E were almost identical in shape and size to the rat protrusions shown in Figures 1A and 1D. The membrane compositions of the mitochondrial protrusions were also similar between the two species: many protrusions contained the single outer mitochondrial membrane (single arrowheads); only some included both the outer and inner mitochondrial membranes (double arrowheads in Figures 2F–2H). Thus, membrane protrusions are a phylogenetically conserved feature of neuronal mitochondria from the rat to the planarian.

Three-Dimensional Ultrastructure of Mitochondrial Protrusions in Neurons

To further investigate the ultrastructure of the mitochondrial protrusions in a spatial context, we leveraged the opensource 3D EM datasets, such as FIB-SEM (focused ion beam-scanning electron microscopy). In the initial course of this study, we evaluated ~15 different 3D SEM datasets produced from various parts of the brain. Although these datasets achieved the purposes of their original studies, not all of them were adequate for analyzing mitochondrial protrusions. One such example was the mouse CA1 FIB-SEM dataset. The CA1 FIB-SEM dataset has a voxel of 8 × 8 × 8 nm, and using this dataset, we had previously segmented and measured the size of neuronal mitochondria (Delgado et al., 2019). However, the staining quality of the EM images was not sufficient to resolve the double membranes of mitochondria, a requirement for analyzing mitochondrial protrusions (Figure S1). In addition, some minor misalignment in parts of the CA1 FIB-SEM dataset added another obstacle for tracing small cellular structures such as mitochondrial protrusions.

We chose to examine the mouse nucleus accumbens FIB-SEM dataset (Wu et al., 2017; Xu et al., 2017), which has a voxel of 4 × 4 × 4 nm, excellent staining quality, and seamless alignment. Using this dataset, we and others were able to acquire spatial information for neuronal mitochondria (Delgado et al., 2019; Wu et al., 2017). For investigating mitochondrial protrusions, as illustrated in Figures 3 and S2, this dataset offered well-resolved fine details.

Figure 3A shows a mitochondrial protrusion (arrowheads) in sequential images in the z direction of a nucleus accumbens neuron. The protrusion, round shaped with a short constricted neck, is the extension of the mitochondrial outer membrane; as the image stacks progress in the z direction, the protrusion appears "detached" from the parent mitochondrion; instead, it adjoins a nearby tubulovesicular structure (arrowheads in Figure 3A; also see Video S1). Figures 3B and 3C show additional examples of mitochondrial protrusions in nucleus accumbens neurons. Figures 3D–3G show examples of mitochondrial protrusions

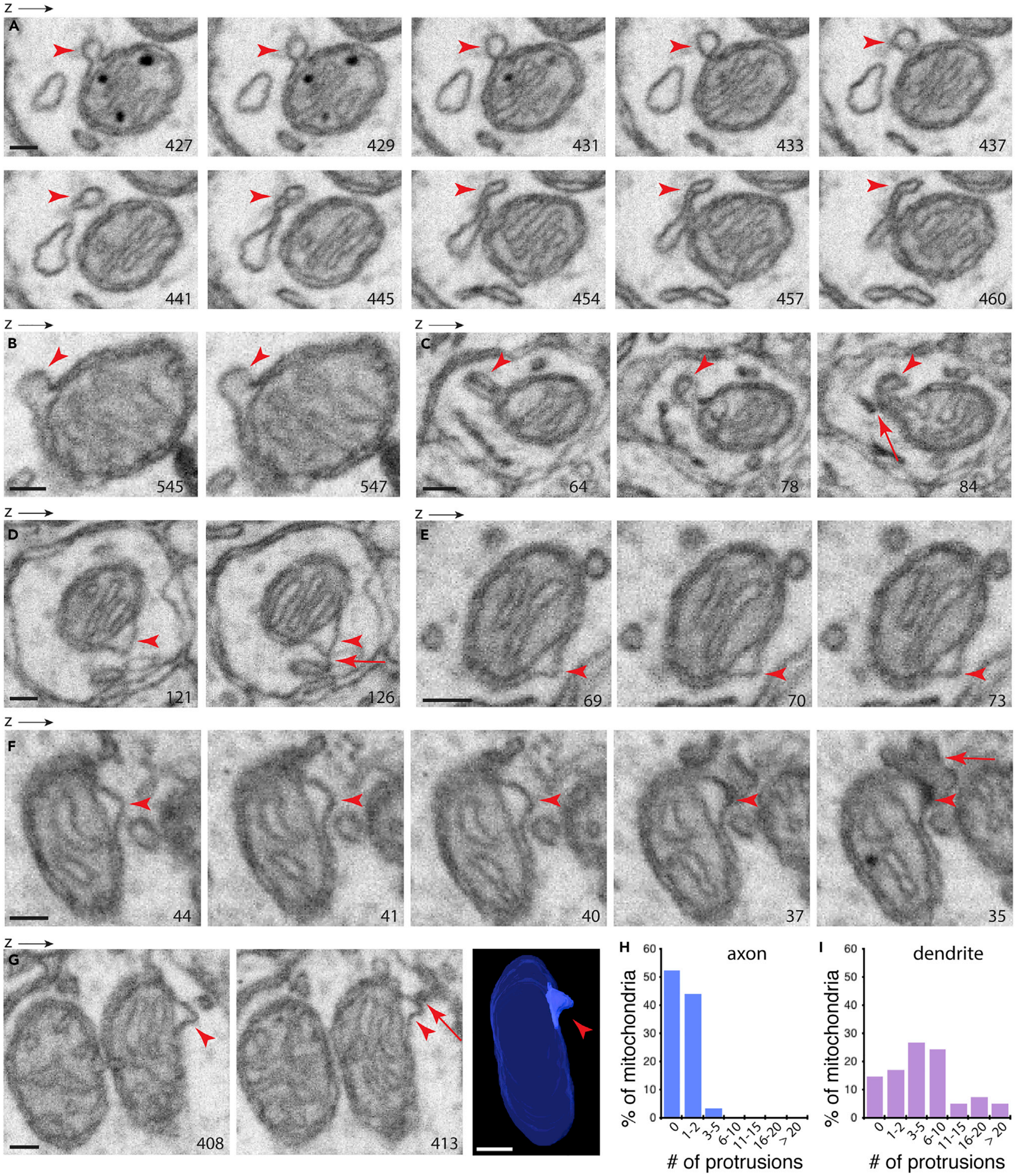

Figure 3. FIB-SEM Analysis of Mitochondrial Protrusions in Neurons of the Mouse Nucleus Accumbens

(A) Selective micrographs showing the spatial progression of a mitochondrial protrusion (arrowheads) connecting to a nearby tubulovesicular structure. The z resolution of the FIB-SEM for the nuclear accumbens is 4 nm. The number on the micrograph indicates its z position in the SEM image stack. A complete stack of consecutive micrographs for this mitochondrial vesicle is shown in Video S1.

(B and C) Examples of mitochondrial protrusions. Note in (C), the mitochondrial protrusion touches a tubular structure (arrow).

Figure 3. *Continued*

(D–G) Additional examples of mitochondrial protrusions, all of which have a stubby neck (arrowheads). Arrow in (D) indicates the tip of the protrusion making direct contact with a nearby tubular structure. Arrow in (F) indicates a part of the protrusion contacting a structure that has the structural feature of a recycling endosome. Arrow in (G) indicates also the tip of the protrusion making contact with a tubular structure. A 3D reconstruction of this mitochondrial protrusion is shown, and a Video showing a complete EM image stack of this example is in Video S2.

(H) Percentage of mitochondria with protrusions. A total of 58 axonal mitochondria and 42 dendritic mitochondria were examined in their entirety in z dimensions. Additional examples of mitochondrial protrusions in the nucleus accumbens are shown in Figure S3. Scale bars, 100 nm.

that do not exhibit constricted necks. Notably, some of these protrusions seemed to be in direct contact with neighboring tubular structures (arrows in Figures 3C, 3D, and 3G and Video S2). Also, as shown in Figure 3F, the tip of the mitochondrial protrusion (arrowheads) contacted a structure that displays features of a recycling endosome (arrow).

To quantify the prevalence of mitochondrial protrusions in nucleus accumbens neurons, we inspected a total of 58 axonal mitochondria and 42 dendritic mitochondria in their entirety in z dimensions. We focused our investigation on two neuronal compartments, axons and dendrites, which were defined on the basis of their continuity to the synapse (Figures S2E and 2F). Approximately 50% of axonal mitochondria had protrusions, whereas nearly 85% of dendritic mitochondria had protrusions and many mitochondria had more than one protrusion (Figures 3H and 3I). Note that we did not include in our analysis small vesiculate structures that did not exhibit unambiguous connections to any mitochondria, despite being in the immediate vicinity of mitochondria (Figure S2).

We next examined a mouse somatosensory cortex dataset produced using ATUM-SEM (automatic tape-collecting ultramicrotome-scanning electron microscopy); this dataset consists of 1,850 aligned images with a voxel of 6 × 6 × 30 nm (Kasthuri et al., 2015). We focused on examining mitochondria in neurons. Figure 4A shows a single image from the cortex ATUM-SEM image stack that includes several mitochondria in axons or dendrites. One mitochondrion has a small bubble-like structure protruding outward (red box in Figure 4A). Following this mitochondrion on sequential images in z dimensions (arrowheads in Figure 4A), the neck of the protrusion is first seen constricted; on the following image, the protrusion appears as a vesicle separating from the mitochondrion. Figure 4B shows three different protrusions from the same mitochondrion. Figures 4C–4E and Figure S4 illustrate additional examples of mitochondrial protrusions. We inspected a total of 400 axonal mitochondria and 200 dendritic mitochondria in their entirety in z dimensions for the presence and the number of mitochondrial protrusions. Interestingly, we found that ~10% of axonal mitochondria had protrusions, whereas ~80% of dendritic mitochondria had protrusions (Figures 4F and 4G). Our analysis possibly underestimated the total number of the protrusions, as the 30-nm z resolution of the cortex ATUM-SEM dataset is likely insufficient to reveal a fraction of the small mitochondrial protrusions.

We next examined the neuropil of the *Drosophila* protocerebral bridge, a brain region involved in coordinating locomotor behavior. The FIB-SEM dataset of the *Drosophila* protocerebral bridge has a voxel of 4 × 4 × 4 nm as well as superior staining quality and precise alignment (Xu et al., 2017), thus enabling the resolution of fine details of mitochondrial protrusions and allowing us to distinguish between protrusions and vesicles that sit next to mitochondria (i.e., Figures S2C and S2D). Figure 5A illustrates a mitochondrial protrusion in a presynaptic terminal, for which synaptic vesicles (sv) and a T-bar (T) are readily visible. The mitochondrial protrusion (upper arrowheads) is clearly seen to be derived from the mitochondrial outer membrane. Interestingly, the tip portion of this protrusion (lower arrowheads) extends to the synapse, almost to the midst of synaptic vesicles and the T-bar. Figure 5B is another example of a presynaptic mitochondrion, although the protrusion itself (arrowheads) is seen at 60–70 nm away from the synapse. Figure 5C shows two dendritic mitochondria with different shapes: one is round with a constricted neck (left arrowheads), and the other has a wide base (right arrowheads); notably, both protrusions are composed of the single outer membrane of the parent mitochondrion. Figures 5D–5H are additional examples of protrusions found on dendritic mitochondria. Interestingly, these dendritic mitochondrial protrusions are either positioned close to the synapse (arrowheads in Figures 5D and 5E) or are situated at the base of thin dendritic processes (arrowheads in Figures 5F–5H).

In previous studies of rat and mouse neurons, axonal mitochondria were found to be several folds smaller than dendritic mitochondria (Chicurel and Harris, 1992; Delgado et al., 2019; Kasthuri et al., 2015; Li et al., 2004; Popov et al., 2005). We thus sought to assess whether mitochondria in the protocerebral bridge neurons of *Drosophila* followed the same size pattern. Accordingly, we measured and compared the size of axonal and dendritic mitochondria. Unlike what has been observed in mammalian neurons, axonal

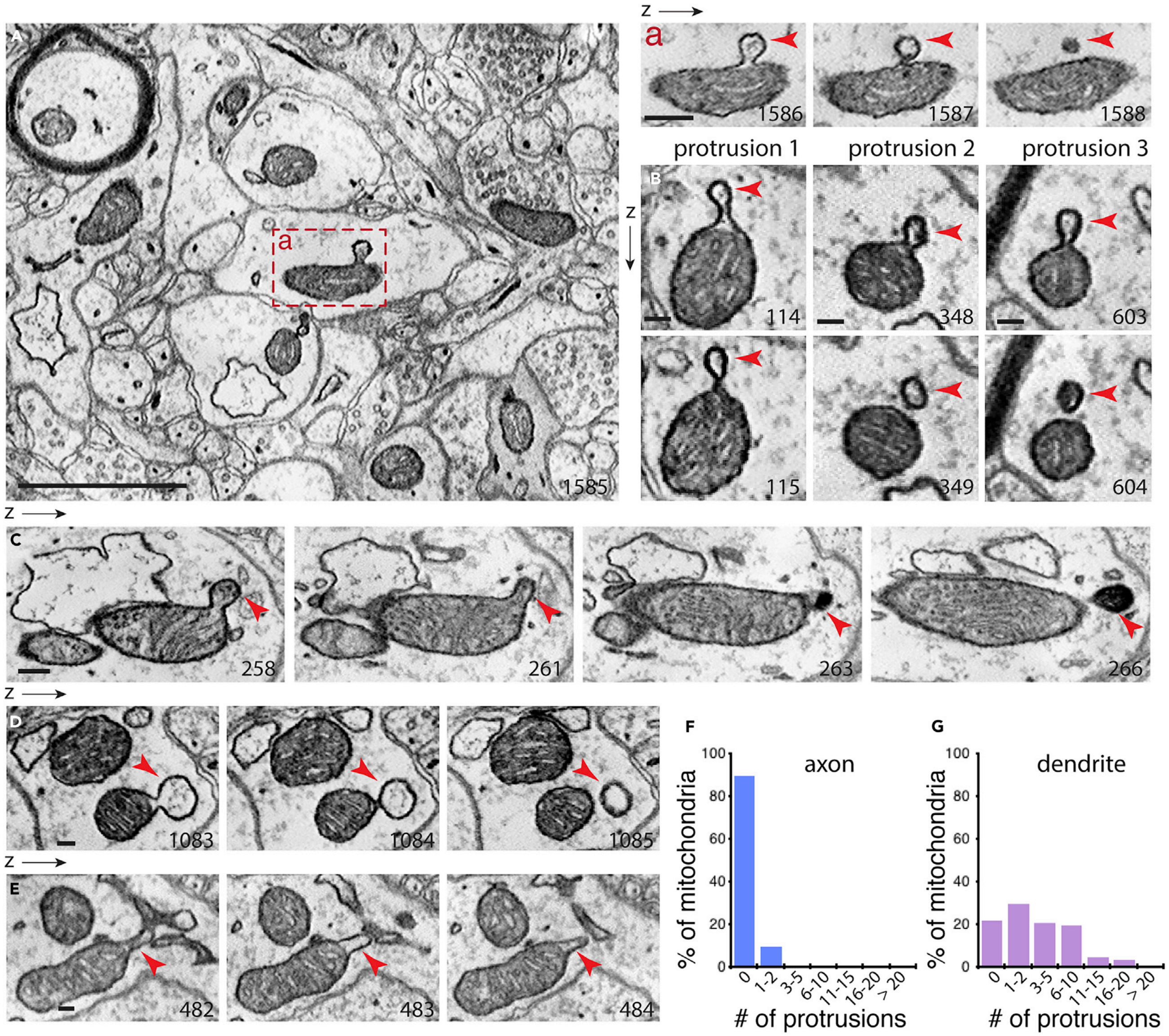

Figure 4. ATUM-SEM Analysis of Mitochondrial Protrusions in Neurons of the Mouse Cortex

(A) A representative micrograph showing mitochondria in axonal or dendritic compartments of neurons. Box-a shows a mitochondrion with a protrusion (arrowheads); note that the tip but not neck of this protrusion stays visible in subsequent micrographs in the z direction (arrowheads). The z resolution of the ATUM-SEM for the cortex is 30 nm. The number on the micrograph indicates its z position in the SEM image stack.

(B) Micrographs showing three different protrusions from the same mitochondrion, as shown in Aa.

(C) An example of a mitochondrial protrusion (arrowheads) and a part of this protrusion is high density (dark).

(D and E) Additional examples illustrating mitochondrial protrusions in different shapes and sizes (arrowheads).

(F and G) Percentage of mitochondria with protrusions. A total of 400 axonal mitochondria and 200 dendritic mitochondria were examined in their entirety in z dimensions.

Scale bar in (A), 1 μm; scale bars in a, and (B)–(E), 100 nm. A 3D reconstruction of the mitochondrion shown in a, and additional examples of protrusions are shown in Figure S4.

mitochondria of the protocerebral bridge neurons were not smaller but rather significantly larger than dendritic mitochondria (axonal $0.55\mu m^3 \pm 0.11$ versus dendritic $0.21\mu m^3 \pm 0.03$, $p = 0.0076$, $n = 20$; Figure S5A). We next assessed whether a correlation exists between the number of the protrusions and the mitochondrial size. In the axon of protocerebral bridge neurons, the protrusion number was moderately correlated with mitochondrial size ($r = 0.494$, $p = 0.027$, $n = 20$); there was no significant correlation for those in dendrites (Figure 5I).

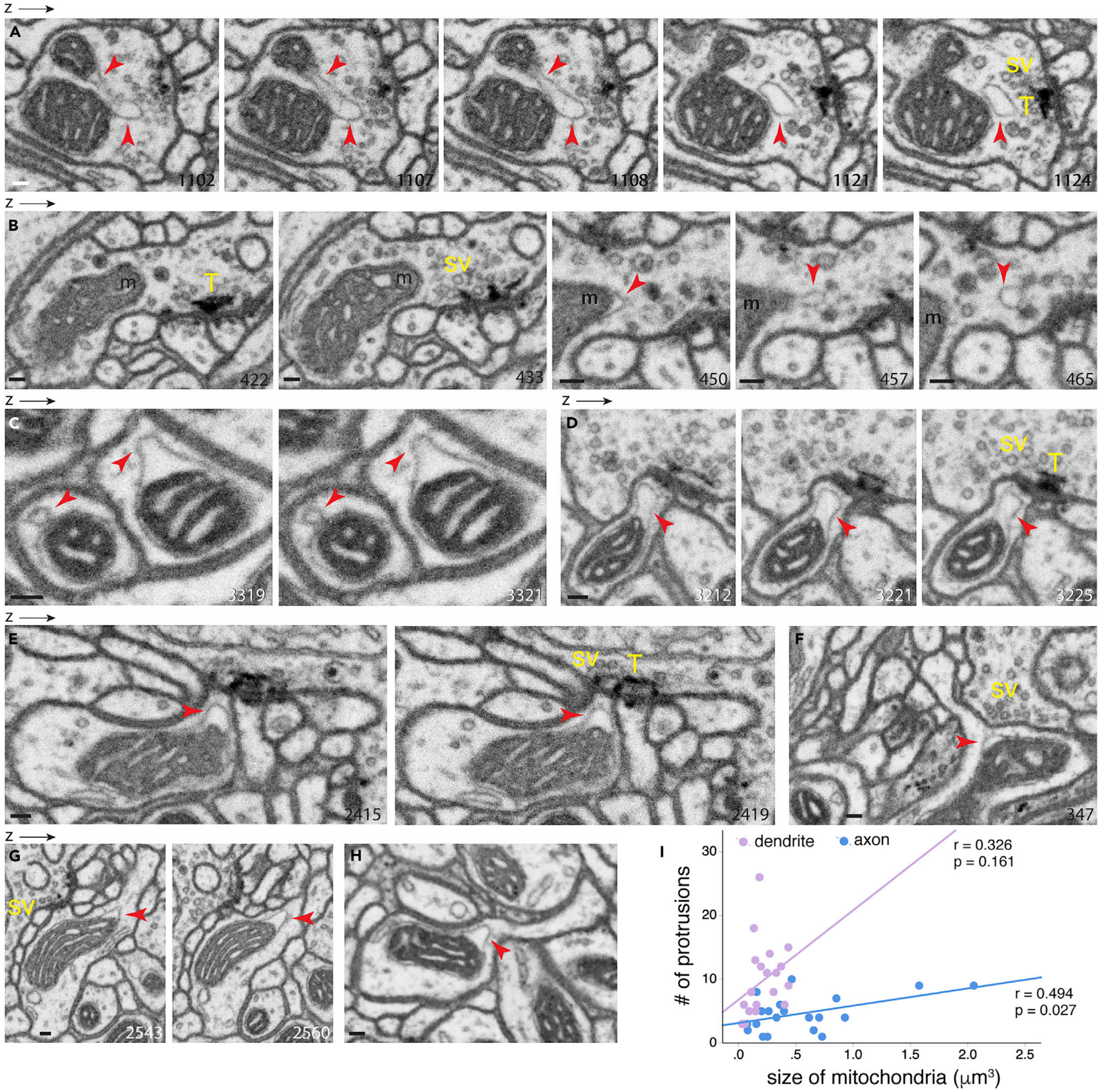

Figure 5. FIB-SEM Analysis of Mitochondrial Protrusions in Neurons of the *Drosophila* Protocerebral Bridge

(A) Micrographs showing spatial progression of a mitochondrial protrusion (arrowheads) in the axonal terminal of a protocerebral bridge neuron. Notice the proximity of the protrusion to the clearly visible synaptic vesicles (sv) and T-bar (T)—the characteristics of the *Drosophila* presynaptic terminal.

(B) Another example of a mitochondrion with a protrusion (arrowheads) in the axonal terminal.

(C) Commonly observed mitochondrial protrusion types—protrusion with a constricted neck (left arrowheads) or with a stubby neck (right arrowheads). In both examples, the protrusions are extensions of mitochondrial outer membranes.

(D and E) Examples illustrating mitochondrial protrusions (arrowheads) in dendrites. The protrusions are positioned immediately at the postsynaptic side of the synapse, as evidenced by the opposing presynaptic T-bar (T) and synaptic vesicles (sv).

(F–H) Examples of dendritic mitochondria whose protrusions (arrowheads) are situated at the base of the neck of a postsynaptic process.

(I) Correlation between number of mitochondrial protrusions and mitochondrial size. Pearson's correlation analysis was used for calculating the r and p values.

The z resolution of the FIB-SEM for the *Drosophila* protocerebral bridge is 4 nm. The number on the micrograph indicates its z position in the SEM image stack. Scale bars, 100 nm. sv, synaptic vesicles; T, presynaptic T-bar.

We also examined the *Drosophila* mushroom body FIB-SEM dataset, which has been used in reconstructing synaptic connections and in revealing new classes of synapses (Takemura et al., 2017). Although we found examples of mitochondrial protrusions (Figures S5C–S5E), the quality of the EM images did not allow in-depth structural and spatial analysis of mitochondrial protrusions.

Mitochondrial Protrusions and Vesicles in Primary Hippocampal Cultures

We extended our studies to mitochondria in dissociated rat hippocampal neuronal cultures. We transiently expressed mito-RFP (a mitochondrial matrix marker) and tom20-YFP (mitochondrial outer membrane marker) in a sparse population of cultured neurons. We used confocal fluorescence microscopy with Airyscan to visualize mitochondria and mitochondrial membrane-derived protrusions and vesicles (Figure 6A). We defined protrusions as tom20-YFP-illuminated structures protruding from, but still connecting to, the parent mitochondria (arrowheads in Figures 6 and S6), and vesicles as tom20-YFP puncta in the vicinity of, but not connecting to, mitochondria (arrows in Figures 6 and S6).

Box 1 in Figure 6B shows examples of budding protrusions that are still connected to mitochondria (arrowheads). Box 2 in Figure 6B shows vesicles that are separated from mitochondria. We noticed that some vesicles (i.e., low arrow in box 2) appeared to form complex tubulovesicular structures, consistent with some of the extensive protrusions seen with EM. Figures 6C and 6D illustrate protrusions with stubby or slender necks. Box 4 in Figure 6C shows a small piece of mitochondrion in the process of fission from the main portion of the mitochondrion joined by a narrow bridge (two opposing arrowheads). The locations of the protrusions in relation to the parent mitochondria varied; some were on the side, whereas others were at the end of the mitochondria (for example, Figures 6D and 6E). Inspecting these protrusions and vesicles in individual RGB channels, we found that most of them contained the tom20-YFP-illuminated outer mitochondrial membrane. Occasionally, we observed protrusions containing both tom20-YFP and mito-RFP. Figure 6F and its enlarged view illustrate an example of a protrusion containing both tom20-YFP and mito-RFP, which is strikingly similar to a mitochondrial protrusion containing the outer membrane and components of inner mitochondrial structures found in the cortex ATUM-SEM dataset (Figure 6G).

We next examined the abundance of mitochondrial protrusions and vesicles in neurons under normal basal condition and in neurons after mild stress. We focused our analysis on the tom20-YFP-illuminated protrusions and vesicles. Previous studies have shown that Antimycin A (AA), an inhibitor of complex III of the mitochondrial electron transport chain, when used at micromolar levels in cell lines or in purified bovine heart mitochondria, stimulated formation of the mitochondria-derived vesicles that selectively carry mitochondrial outer membrane proteins including tom20 (Soubannier et al., 2012a, 2012b). Experiments carried out in cultured neurons showed that a low dose (nanomolar range) of Antimycin A induced a mild and reversible mitochondrial stress without eliciting mitophagy (Lin et al., 2017). Accordingly, we used the mild-stress protocol by treating the neurons with 5 nM of Antimycin A for 5 h before assessing their mitochondria. Despite neuron-to-neuron and mitochondria-to-mitochondria variations, values averaged over 100 fluorescence images (67.8 μm^2 per image) from five independent experiments (a total of 2054 mitochondria) exhibited a clear difference: mitochondria in the Antimycin A-treated neurons had significantly more mitochondrial protrusions and vesicles compared with the basal untreated control (protrusions: control 0.123 ± 0.012 versus AA-treated 0.241 ± 0.036, $p = 0.0032$, $n = 50$; vesicles: control 0.341 ± 0.036 versus AA-treated 1.038 ± 0.216, $p = 0.0025$, $n = 50$; Figures 6H, 6I, and S6). The number or size of mitochondria themselves, on the other hand, remained unchanged in Antimycin A-stressed neurons (Figures 6J and 6K).

DISCUSSION

Using TEM, 3D SEM, and confocal fluorescence microscopy with Airyscan to visualize mitochondria, we have characterized mitochondrial membranous protrusions and vesicles in neurons of multiple species. The three approaches used in this study—2D EM, 3D EM, and high-resolution light microscopy of fluorescent mitochondrial markers—uncovered different facets of these protrusions and vesicles. The TEM analysis of the rat and planarian brain showed similar ultrastructural features of mitochondrial protrusions in two phylogenetically distant species, albeit no spatial information was revealed and the sampling size was limited. These limitations were overcome by analysis of 3D SEM, which elucidated the nanoscale details of the mitochondrial protrusions and their spatial relationship to some of the surrounding cellular structures. Furthermore, the 3D SEM allowed assessment of the proportion of the protrusion-bearing mitochondria in the brain and the frequency of the protrusions across entire mitochondria. Fluorescence microscopy of mitochondrial markers complemented the EM

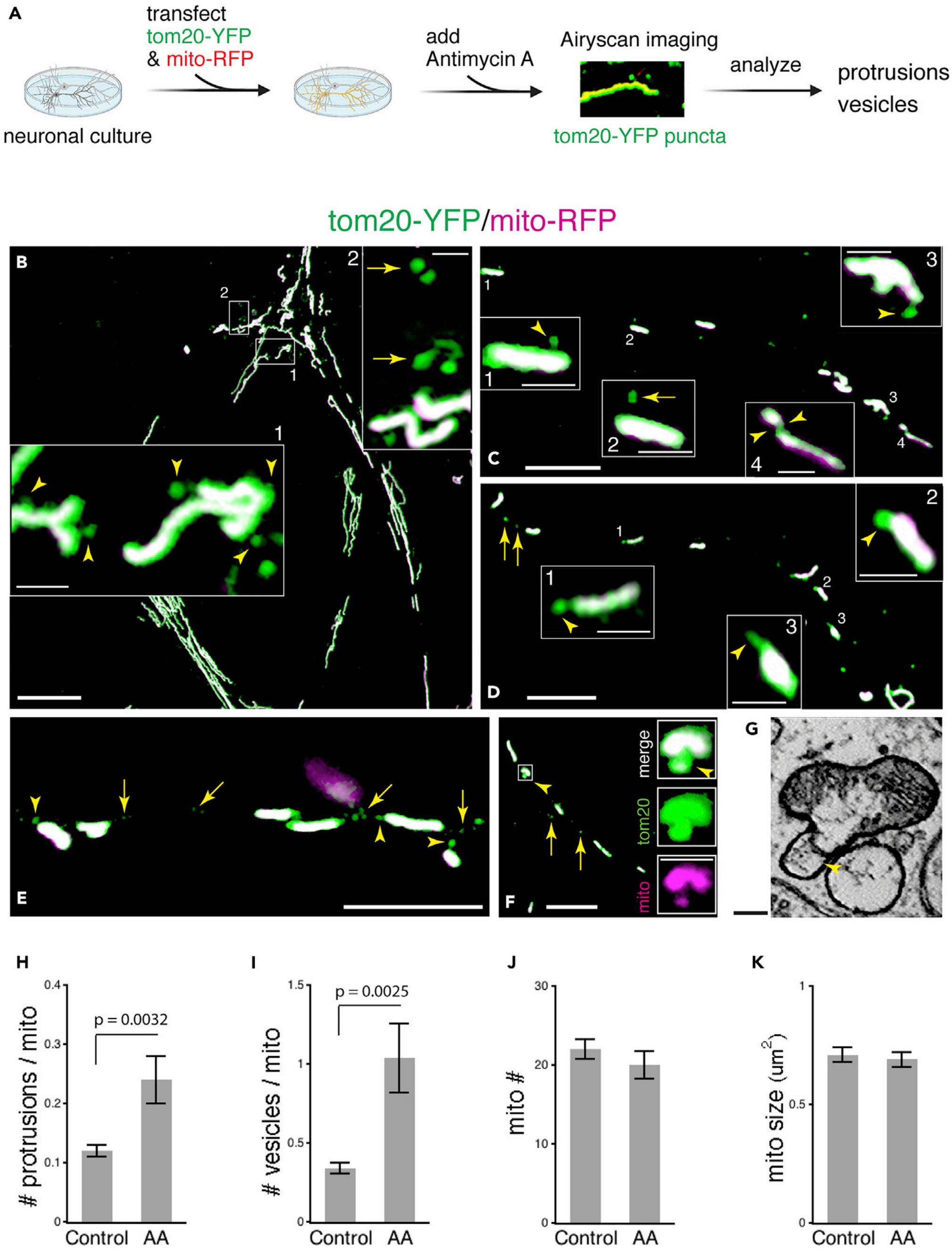

Figure 6. Fluorescence Light Microscopy Reveals Mitochondrial Protrusions and Vesicles in Hippocampal Neurons and Higher Incidence of the Protrusions and Vesicles in Neurons Under Mild Stress

(A) Experiment and analysis used to assess mitochondrial protrusions and vesicles in cultured hippocampal neurons.

(B) Fluorescence image of cultured hippocampal neurons expressing tom20-YFP and mito-RFP. The enlarged view in box 1 shows examples of tom20-YFP-illuminated mitochondrial protrusions (arrowheads). The protrusions are connected to mitochondria through either slender or stubby necks. The enlarged view in box 2 shows examples of tom20-YFP mitochondrial vesicles, which are detached from mitochondria (arrows).

(C) Boxes 1 and 3 show sample mitochondrial protrusions (arrowheads); box 2 shows a mitochondrial vesicle (arrow). Box 4 shows a small piece of mitochondrion in the process of fission from the main portion of the mitochondrion joined by a narrow bridge (two opposing arrowheads).

(D) Additional examples of mitochondrial protrusions (arrowheads) and vesicles (arrows). Enlarged views (boxes 1–3) illustrate mitochondrial protrusions in a variety of shapes.

Figure 6. *Continued*

(E) Examples of mitochondrial protrusions (arrowheads) and vesicles (arrows). Note that the protrusions appear to be budding from the ends of mitochondria.

(F and G) A mitochondrial protrusion (arrowhead) including both tom20-YFP and mito-RFP revealed by light microscopy (enlarged view of individual RGB channels in F); this protrusion is strikingly similar to a mitochondrial protrusion containing the outer membrane and components of inner mitochondrial structures revealed by ATUM-SEM in a mouse cortical neuron (G).

(H and I) Number of tom20-YFP-mitochondrial protrusions or vesicles per mitochondrion.

(J and K) Number and size of mitochondria expressing tom20-YFP and mito-RFP. AA, Antimycin A (5 nM for 5 h); control, untreated.

For (H–K), data are represented as mean ± SEM; n = 50 fluorescence images (67.8 μm^2 per image) for each condition from five independent experiments. Student's t test was used for calculating all the p values. All images shown are neurons treated with AA. Additional fluorescence images of AA-treated and untreated controls are shown in Figure S6. Scale bars in (B), 10 μm; in (C)–(F), 5 μm; in all boxed views, 1 μm; in (G), 100 nm.

analyses, as it offered an evaluation of the abundance of the mitochondrial protrusions and vesicles in neurons in normal conditions and after mild mitochondrial stress.

Many 3D SEM datasets have been produced for the brain in recent years. These datasets have provided a powerful tool for understanding the complexity of the brain at the cellular and subcellular levels (Bock et al., 2011; Kasthuri et al., 2015; Lee et al., 2016; Takemura et al., 2017; Tomassy et al., 2014; Wang et al., 2020; Wanner et al., 2016). Investigating mitochondrial protrusions or vesicles, however, poses high demands in terms of voxel resolutions and EM image quality. Image stacks with a z resolution of 50 nm or more likely fail to reveal populations of small protrusions. Datasets with high voxel resolutions, but without adequate staining or alignment, are also insufficient to resolve fine details of mitochondria and their protrusions (for example, Figure S1).

Among the FIB-SEM datasets we analyzed in this study, the mouse nucleus accumbens (Wu et al., 2017; Xu et al., 2017) and *Drosophila* protocerebral bridge (Xu et al., 2017) have superior image quality. In spite of their high voxel resolution (4 × 4 × 4 nm for both), excellent staining, and precise alignment, there is no time dimension; thus, we were unable to distinguish between vesicles that were derived from mitochondria and vesicles that were to fuse with mitochondria or potentially non-mitochondrial vesicles that happened to be nearby. For this reason, we focused our attention on mitochondrial protrusions, which had an unambiguous relationship to mitochondria, and observed the following characteristics. First, regarding shape, some protrusions have narrow constricted necks at their bases, whereas others have wide bases exhibiting a feature similar to the wide-based "blebs" described in a previous study of mitochondria-derived vesicles in non-neuronal cells (Sugiura et al., 2014). Second, regarding size, there seem to be two categories: small ones at a size of 50–150 nm in the x and y plane and visible only across a few images in the z directions and large ones, which can be traced across many images in z directions and often are found to be a part of nearby tubulovesicular structures (for additional examples, see Videos S1, S3, S4, and S5). Third, regarding membrane structure, it is interesting to note that the majority of the mitochondria we have observed extended from the single outer mitochondrial membrane.

To complement the EM findings, we used fluorescence microscopy to examine mitochondria in cultured neurons expressing tom20-YFP. We reasoned that we could use mitochondrial outer membrane protein tom20 to decipher protrusions (still attached to the parent mitochondria) and vesicles (have detached from mitochondria) (Figures 6 and S6). Using this system, we determined basal amounts of mitochondrial protrusions and vesicles in neurons and their substantially higher abundance in neurons in response to Antimycin A-induced stress. Whether the stress-elicited prevalence of mitochondrial vesicles observed in cultured neurons can be expanded to the brain and neurons *in vivo* awaits future investigation.

The findings of this study suggest that generation of protrusions and vesicles is an important aspect of mitochondrial function under normal and pathological conditions. Future studies combining techniques with high spatial and temporal resolutions are required to reveal the functional implications of mitochondrial protrusion and vesicle production in neurons and their potential implication in disease pathogenesis.

Limitations of the Study

This study had several strengths, and also paired limitations. First, we have examined mitochondrial protrusions using TEM and 3D SEM and revealed similar ultrastructural features in neuronal cells from rodent to planarian to *Drosophila*. It will be informative to also examine the interaction or physical contact between mitochondrial protrusions and other cellular organelles including but not limited to endosomes, lysosomes, and peroxisomes. Second, we examined two neuronal compartments, axons and dendrites, revealing commonalities, and also differences that may reflect different functions and quality control mechanisms. It will be useful to also examine mitochondria and their protrusions in the soma of neurons and in other brain cells including glia and cells of the blood-brain barrier. Third, we noticed a seemingly differential prevalence of mitochondrial protrusions in axons versus dendrites. Given that mitochondria in axons and dendrites have difference sizes, it will be valuable to determine, if in fact, the size or site of mitochondria determines the prevalence of these protrusions. More broadly, future studies should explore factors, constitutional traits of different neuronal compartments, and cellular functional states that may dictate the formation of mitochondrial protrusions. Fourth, our TEM and 3D SEM analyses could only identify protrusions but not bona fide mitochondria-derived vesicles. It will be important to investigate which and when mitochondrial protrusions progress toward mitochondrial vesicles. Finally, we investigated the abundance of mitochondrial protrusions and vesicles in neurons under mild stress. It will be critically important to understand the functions of mitochondrial vesicles in normal and pathological neurons.

Resource Availability

Lead Contact

Further information and requests for resources and reagents should be directed to and fulfilled by the Lead Contact, Pamela J. Yao (Pamela.Yao@nih.gov).

Materials Availability

This study did not generate new unique reagents.

Data and Code Availability

The published article includes all datasets analyzed during the study.

METHODS

All methods can be found in the accompanying Transparent Methods supplemental file.

SUPPLEMENTAL INFORMATION

Supplemental Information can be found online at https://doi.org/10.1016/j.isci.2020.101514.

ACKNOWLEDGMENT

We would like thank Dr. Harald F. Hess for providing nucleus accumbens FIB-SEM dataset and helpful discussions and Dr Harald F. Hess and Dr. Shan C. Xu for providing *Drosophila* protocerebral bridge and mushroom body FIB-SEM datasets. We thank Dr. Daniel R. Berger for valuable assistance with the annotating software VAST. We also thank Dr. Carolyn Ott, Dr. Jennifer Lippincott-Schwartz, and Dr. Chad Williamson for reagents and insightful discussions. This study was supported by the Intramural Research Programs of NIA, NIH, and NIDCD, NIH. The Advanced Imaging Core code is ZIC DC000081.

AUTHOR CONTRIBUTIONS

P.J.Y. designed experiments; P.J.Y., R.S.P., E.E., J.W.G., and Y.-X.W. conducted experiments; P.J.Y., R.S.P., E.E., and D.K. analyzed data; P.J.Y. wrote the manuscript; R.S.P. and D.K. edited the manuscript; and all authors reviewed the manuscript.

DECLARATION OF INTERESTS

The authors declare no competing interests.

Received: April 14, 2020
Revised: July 15, 2020
Accepted: August 25, 2020
Published: September 25, 2020

REFERENCES

Abuaita, B.H., Schultz, T.L., and O'Riordan, M.X. (2018). Mitochondria-derived vesicles deliver antimicrobial reactive oxygen species to control phagosome-localized *Staphylococcus aureus*. Cell Host Microbe *24*, 625–636.

Ashrafi, G., de Juan-Sanz, J., Farrell, R.J., and Ryan, T.A. (2020). Molecular tuning of the axonal mitochondrial Ca2+ uniporter ensures metabolic flexibility of neurotransmission. Neuron *105*, 678–687.

Bock, D.D., Lee, W.C., Kerlin, A.M., Andermann, M.L., Hood, G., Wetzel, A.W., Yurgenson, S., Soucy, E.R., Kim, H.S., and Reid, R.C. (2011). Network anatomy and in vivo physiology of visual cortical neurons. Nature *471*, 177–182.

Braschi, E., Goyon, V., Zunino, R., Mohanty, A., Xu, L., and McBride, H.M. (2010). Vps35 mediates vesicle transport between the mitochondria and peroxisomes. Curr. Biol. *20*, 1310–1315.

Cadete, V.J., Deschênes, S., Cuillerier, A., Brisebois, F., Sugiura, A., Vincent, A., Turnbull, D., Picard, M., McBride, H.M., and Burelle, Y. (2016). Formation of mitochondrial-derived vesicles is an active and physiologically relevant mitochondrial quality control process in the cardiac system. J. Physiol. *594*, 5343–5362.

Chicurel, M.E., and Harris, K.M. (1992). Three-dimensional analysis of the structure and composition of CA3 branched dendritic spines and their synaptic relationships with mossy fiber boutons in the rat hippocampus. J. Comp. Neurol. *325*, 169–182.

Delgado, T., Petralia, R.S., Freeman, D.W., Sedlacek, M., Wang, Y.X., Brenowitz, S.D., Sheu, S.H., Gu, J.W., Kapogiannis, D., Mattson, M.P., and Yao, P.J. (2019). Comparing 3D ultrastructure of presynaptic and postsynaptic mitochondria. Biol. Open *8*, bio044834.

Gatica, D., Lahiri, V., and Klionsky, D.J. (2018). Cargo recognition and degradation by selective autophagy. Nat. Cell Biol. *20*, 233–242.

Harris, J.J., Jolivet, R., and Attwell, D. (2012). Synaptic energy use and supply. Neuron *75*, 762–777.

Kang, J.S., Tian, J.H., Pan, P.Y., Zald, P., Li, C., Deng, C., and Sheng, Z.H. (2008). Docking of axonal mitochondria by syntaphilin controls their mobility and affects short-term facilitation. Cell *132*, 137–148.

Kasthuri, N., Hayworth, K.J., Berger, D.R., Schalek, R.L., Conchello, J.A., Knowles-Barley, S., Lee, D., Vázquez-Reina, A., Kaynig, V., Jones, T.R., et al. (2015). Saturated reconstruction of a volume of neocortex. Cell *162*, 648–661.

Lee, W.C., Bonin, V., Reed, M., Graham, B.J., Hood, G., Glattfelder, K., and Reid, R.C. (2016). Anatomy and function of an excitatory network in the visual cortex. Nature *532*, 370–374.

Li, Z., Okamoto, K., Hayashi, Y., and Sheng, M. (2004). The importance of dendritic mitochondria in the morphogenesis and plasticity of spines and synapses. Cell *119*, 873–887.

Lin, M.Y., Cheng, X.T., Tammineni, P., Xie, Y., Zhou, B., Cai, Q., and Sheng, Z.H. (2017). Releasing syntaphilin removes stressed mitochondria from axons independent of mitophagy under pathophysiological conditions. Neuron *94*, 595–610.

Matheoud, D., Sugiura, A., Bellemare-Pelletier, A., Laplante, A.,, Rondeau, C., Chemali, M., Fazel, A., Bergeron, J.J., Trudeau, L.E., Burelle, Y., et al. (2016). Parkinson's disease-related proteins PINK1 and parkin repress mitochondrial antigen presentation. Cell *166*, 314–327.

McLelland, G.L., Soubannier, V., Chen, C.X., McBride, H.M., and Fon, E.A. (2014). Parkin and PINK1 function in a vesicular trafficking pathway regulating mitochondrial quality control. EMBO J. *33*, 282–295.

Misgeld, T., and Schwarz, T.L. (2017). Mitostasis in neurons: maintaining mitochondria in an extended cellular architecture. Neuron *96*, 651–666.

Neuspiel, M., Schauss, A.C., Braschi, E., Zunino, R., Rippstein, P., Rachubinski, R.A., Andrade-Navarro, M.A., and McBride, H.M. (2008). Cargo-selected transport from the mitochondria to peroxisomes is mediated by vesicular carriers. Curr. Biol. *18*, 102–108.

Parzych, K.R., and Klionsky, D.J. (2014). An overview of autophagy: morphology, mechanism, and regulation. Antioxid. Redox Signal. *20*, 460–473.

Picca, A., Calvani, R., Coelho-Junior, H.J., Landi, F., Bernabei, R., and Marzetti, E. (2020). Inter-organelle membrane contact sites and mitochondrial quality control during aging: a geroscience view. Cells *9*, 598.

Petralia, R.S., Wang, Y.X., Mattson, M.P., and Yao, P.J. (2015). Structure, distribution, and function of neuronal/synaptic spinules and related invaginating projections. Neuromolecular Med. *17*, 211–240.

Petralia, R.S., Wang, Y.X., Mattson, M.P., and Yao, P.J. (2016). The diversity of spine synapses in animals. Neuromolecular Med. *18*, 497–539.

Pickles, S., Vigié, P., and Youle, R.J. (2018). Mitophagy and quality control mechanisms in mitochondrial maintenance. Curr. Biol. *28*, R170–R185.

Popov, V., Medvedev, N.I., Davies, H.A., and Stewart, M.G. (2005). Mitochondria form a filamentous reticular network in hippocampal dendrites but are present as discrete bodies in axons: a three-dimensional ultrastructural study. J. Comp. Neurol. *492*, 50–65.

Rangaraju, V., Lauterbach, M., and Schuman, E.M. (2019). Spatially stable mitochondrial compartments fuel local translation during plasticity. Cell *176*, 73–84.

Roberts, R.F., Tang, M.Y., Fon, E.A., and Durcan, T.M. (2016). Defending the mitochondria: the pathways of mitophagy and mitochondrial-derived vesicles. Int. J. Biochem. Cell Biol. *79*, 427–436.

Soubannier, V., McLelland, G.L., Zunino, R., Braschi, E., Rippstein, P., Fon, E.A., and McBride, H.M. (2012a). A vesicular transport pathway shuttles cargo from mitochondria to lysosomes. Curr. Biol. *22*, 135–141.

Soubannier, V., Rippstein, P., Kaufman, B.A., Shoubridge, E.A., and McBride, H.M. (2012b). Reconstitution of mitochondria derived vesicle formation demonstrates selective enrichment of oxidized cargo. PLoS One *7*, e52830.

Sugiura, A., McLelland, G.L., Fon, E.A., and McBride, H.M. (2014). A new pathway for mitochondrial quality control: mitochondrial-derived vesicles. EMBO J. *33*, 2142–2156.

Takemura, S.Y., Aso, Y., Hige, T., Wong, A., Lu, Z., Xu, C.S., Rivlin, P.K., Hess, H., Zhao, T., Parag, T., et al. (2017). A connectome of a learning and memory center in the adult Drosophila brain. Elife *6*, e26975.

Tomassy, G.S., Berger, D.R., Chen, H.H., Kasthuri, N., Hayworth, K.J., Vercelli, A., Seung, H.S., Lichtman, J.W., and Arlotta, P. (2014). Distinct profiles of myelin distribution along single axons of pyramidal neurons in the neocortex. Science *344*, 319–324.

Wang, Q., Ding, S.L., Li, Y., Royall, J., Feng, D., Lesnar, P., Graddis, N., Naeemi, M., Facer, B., Ho, A., et al. (2020). The allen mouse brain common coordinate framework: a 3D reference atlas. Cell *181*, 936–953.

Wanner, A.A., Genoud, C., Masudi, T., Siksou, L., and Friedrich, R.W. (2016). Dense EM-based reconstruction of the interglomerular projectome in the zebrafish olfactory bulb. Nat. Neurosci. *19*, 816–825.

Wu, Y., Whiteus, C., Xu, C.S., Hayworth, K.J., Weinberg, R.J., Hess, H.F., and De Camilli, P. (2017). Contacts between the endoplasmic reticulum and other membranes in neurons. Proc. Natl. Acad. Sci. U S A *114*, E4859–E4867.

Xu, C.S., Hayworth, K.J., Lu, Z., Grob, P., Hassan, A.M., García-Cerdán, J.G., Niyogi, K.K., Nogales, E., Weinberg, R.J., and Hess, H.F. (2017). Enhanced FIB-SEM systems for large-volume 3D imaging. Elife *6*, e25916.

Yamashita, A., Fujimoto, M., Katayama, K., Yamaoka, S., Tsutsumi, N., and Arimura, S. (2016). formation of mitochondrial outer membrane derived protrusions and vesicles in *Arabidopsis thaliana*. PLoS One *11*, e0146717.

Youle, R.J. (2019). Mitochondria-Striking a balance between host and endosymbiont. Science *365*, eaaw9855.

iScience, Volume *23*

Supplemental Information

Mitochondrial Protrusions in Neuronal Cells

Pamela J. Yao, Erden Eren, Ronald S. Petralia, Jeffrey W. Gu, Ya-Xian Wang, and Dimitrios Kapogiannis

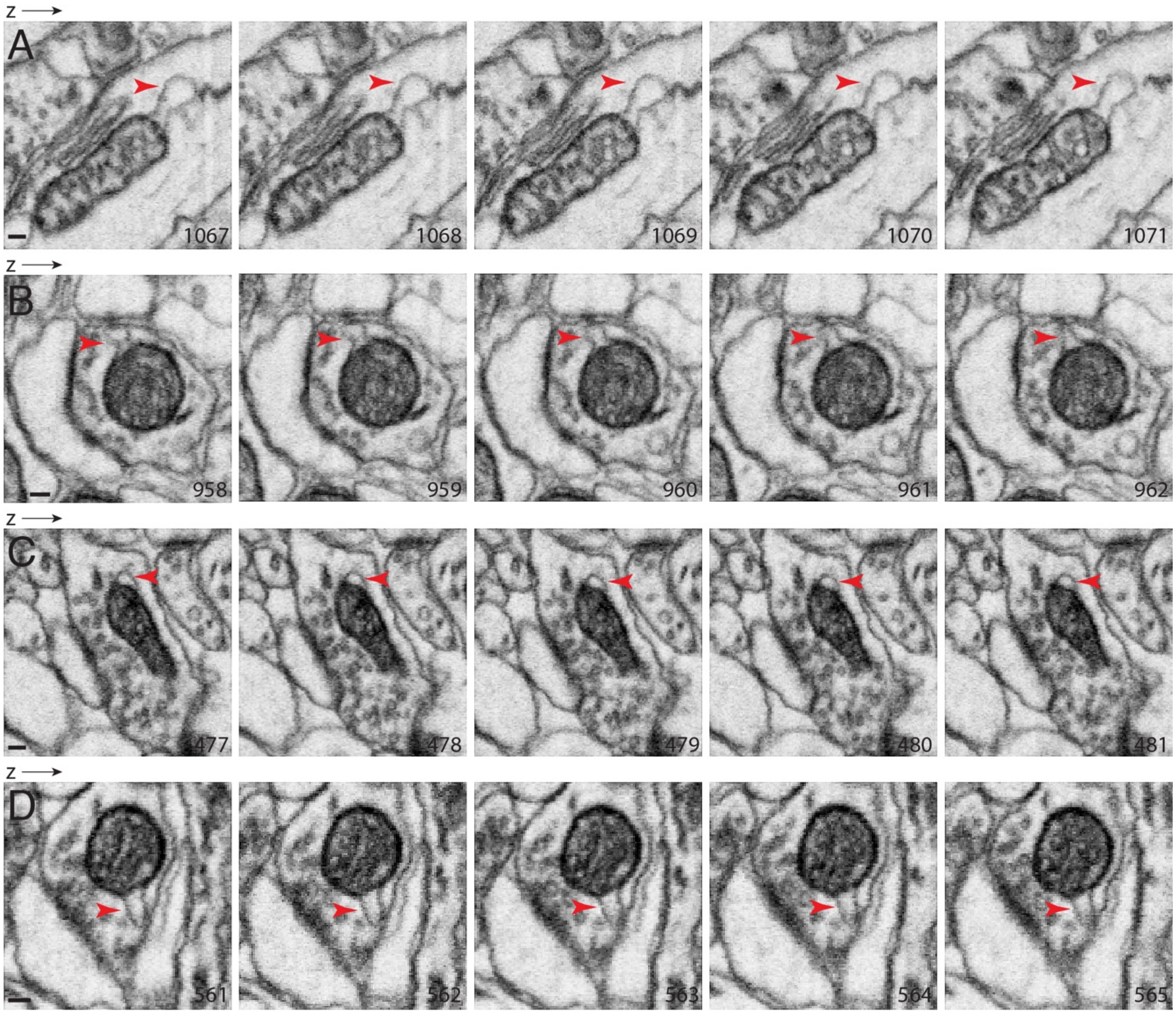

Figure S1. FIB-SEM examination of neurons in the mouse hippocampus (CA1), Related to Figure 3 & 4. (A-D) Examples of mitochondrial protrusions (arrowheads). The voxel of the FIB-SEM is 8x8x8 nm. The number on the micrograph indicates its z-position in the SEM image stack. Scale bars, 100 nm.

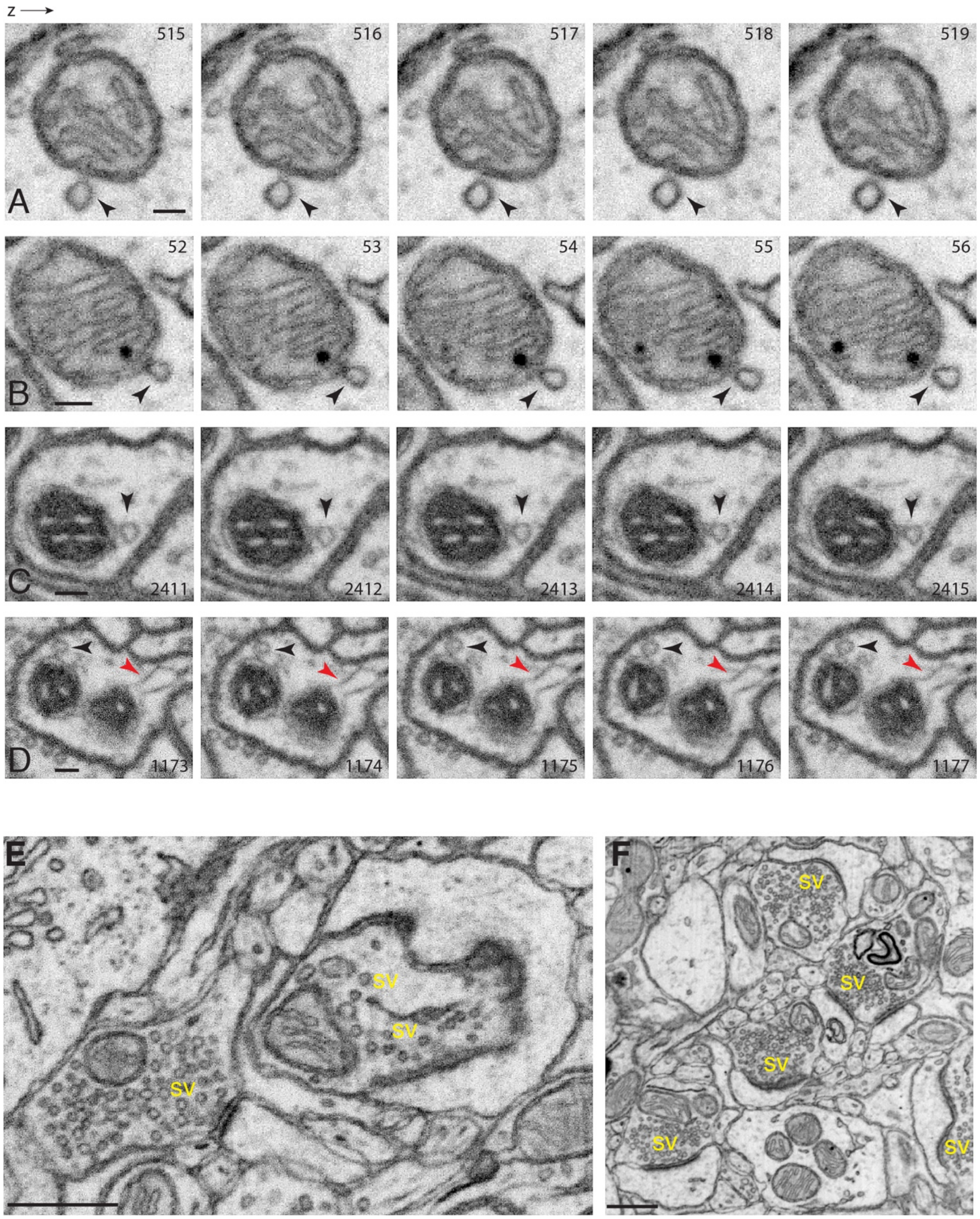

Figure S2. Definition of mitochondrial protrusions, and synapses, Related to Figure 3-5. (A-D) Examples of vesicles (black arrowheads) next to, but not a part of, mitochondria. Unlike the typical mitochondria protrusion (i.e., red arrowheads in D), these next-to-mitochondria-vesicles are not included in the analysis of this study. (A,B) FIB-SEM of the mouse nucleus accumbens. (C,D) FIB-SEM of the *Drosophila* protocerebral bridge. The voxel of both FIB-SEM stacks is 4x4x4 nm. The number on the micrograph indicates its z-position in the SEM image stack. (E,F) Structural features of synapse: presynaptic terminal containing synaptic vesicles (sv), synaptic cleft, and postsynaptic density. Scale bars in A to D, 100 nm, in E,F, 500 nm.

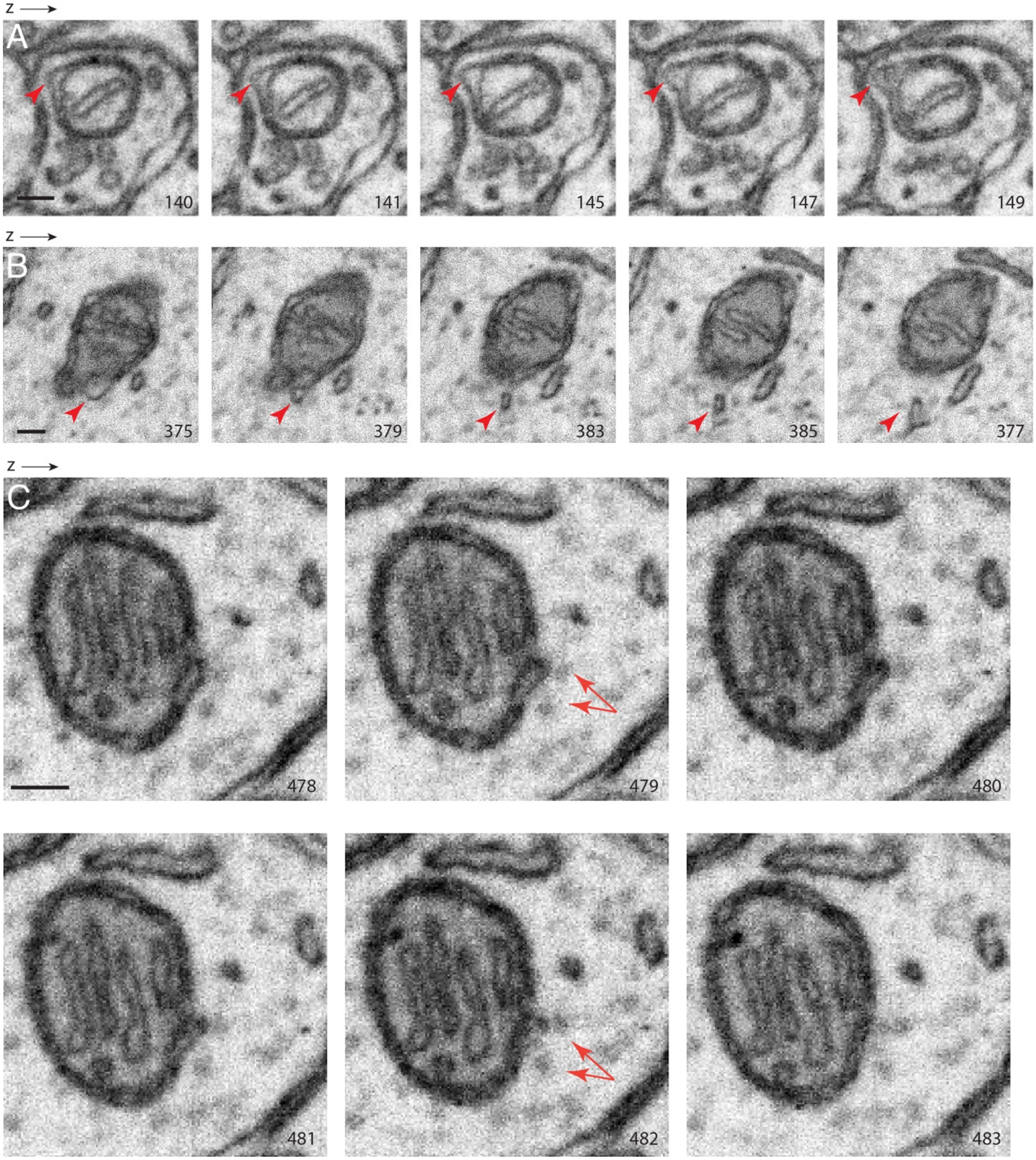

Figure S3. Additional examples of mitochondrial protrusions in neurons of the mouse nucleus accumbens revealed by FIB-SEM, Related to Figure 3. (A) A protrusion with a stubby neck. (B) An example of a small protrusion (arrowheads). (C) In this example, cross-section views of several microtubules are evident; red arrows indicate two of them; note the 1) light color compared to the membrane of adjacent tubulovesicular structures, 2) generally rounded shape in cross-section, and 3) occasional radial spokes. Also shown in this image series, a mitochondrial protrusion makes a direct contact with one of the microtubules (top arrow).The z-resolution of the SEM image stack is 4 nm. The number on the micrograph indicates its z-position in the image stack. Scale bar, 100 nm.

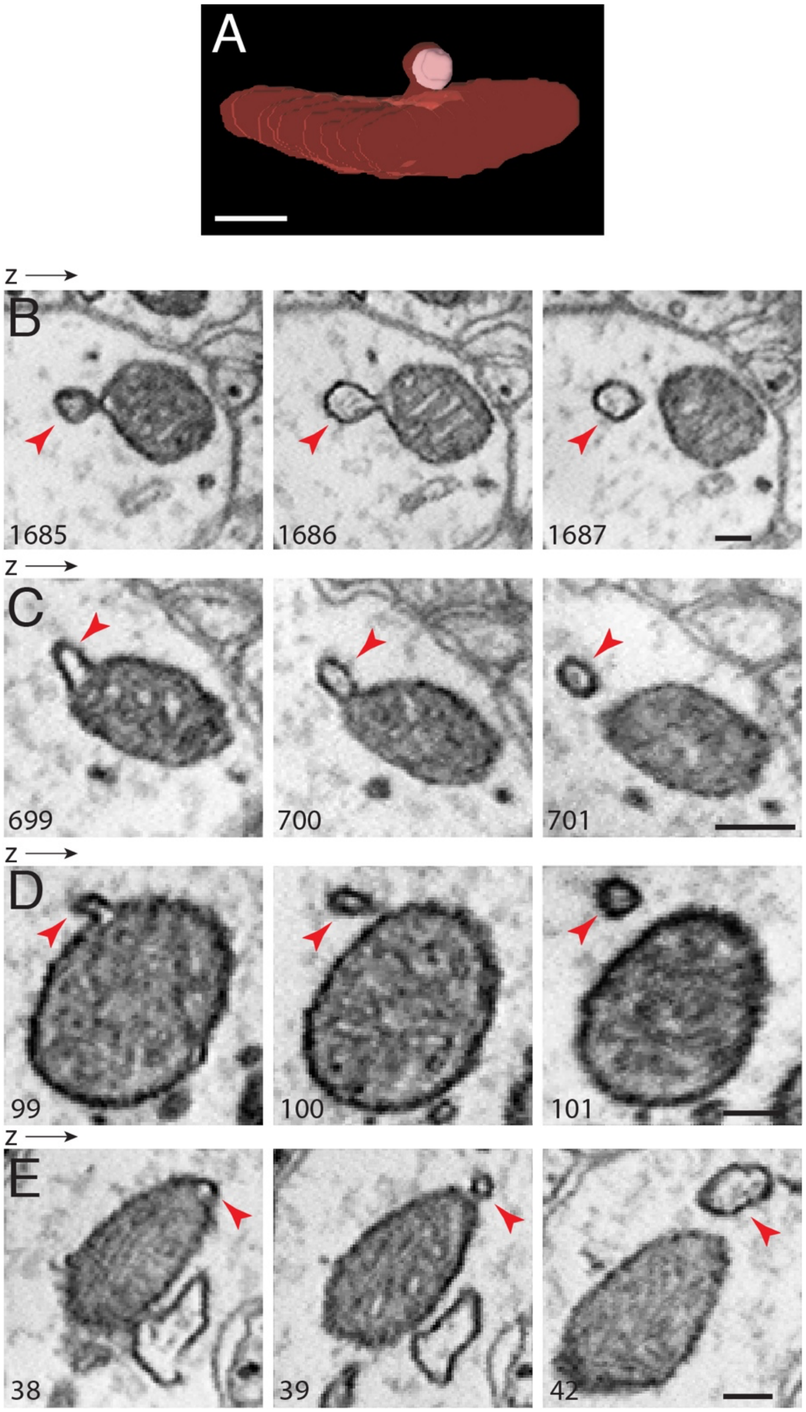

Figure S4. Additional examples of mitochondrial protrusions in neurons of the mouse cortex revealed by ATUM-SEM, Related to Figure 4. (A) A 3D reconstruction of a mitochondrion with a protrusion (see Figure 4A,a). (B-E) Examples showing mitochondrial protrusions in different shapes and sizes. The z-resolution of the EM image stack is 30 nm. The number on the micrograph indicates its z-position in the image stack. Scale bars, 100 nm.

]

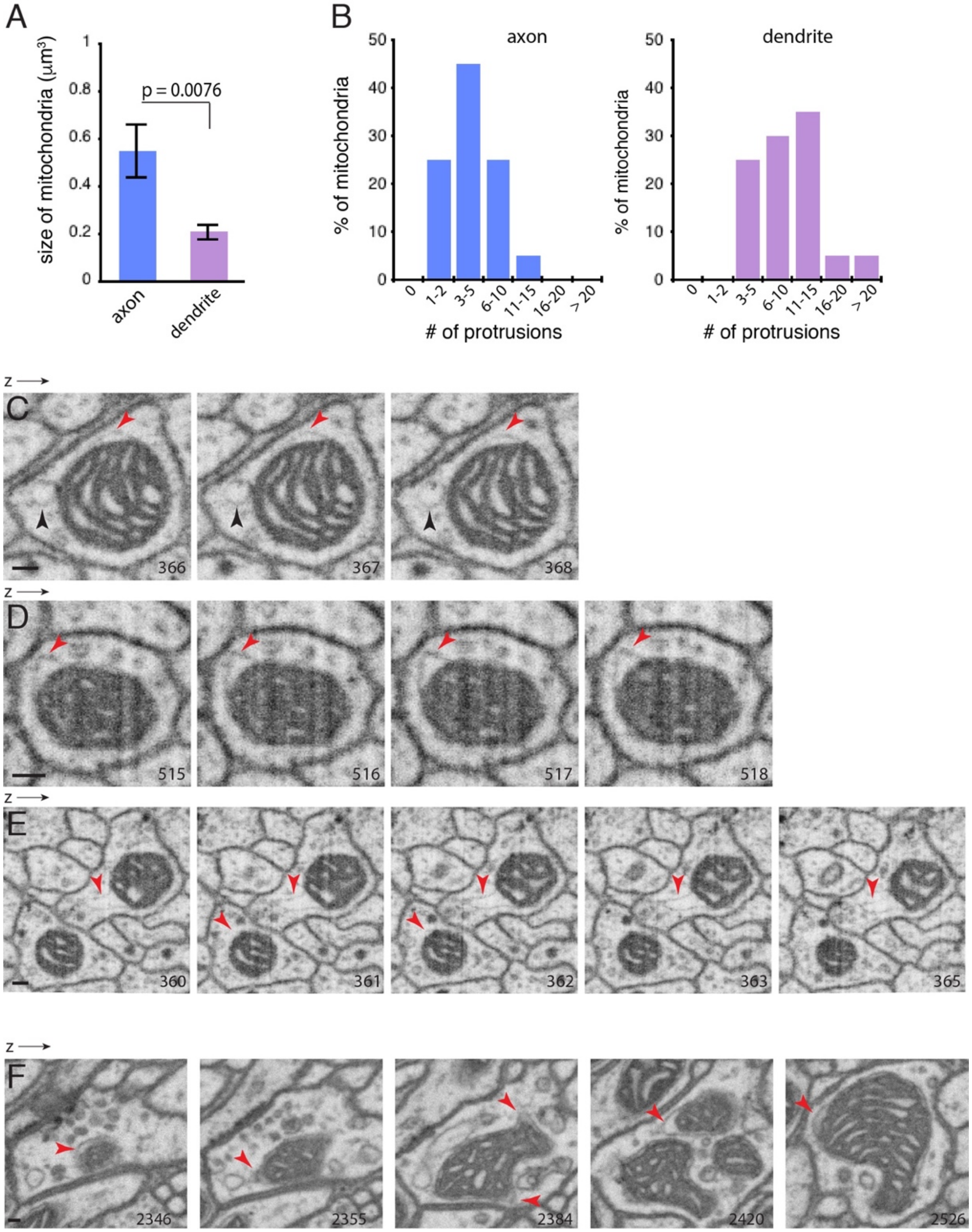

Figure S5. FIB-SEM examination of *Drosophila* neurons, Related to Figure 5. (A,B) Protocerebral bridge neurons. (A) Comparison of the size of axonal and dendritic mitochondria. Data are represented as mean ± SEM. Student's *t* test was used for calculating the p value. n = 20 axonal and 20 dendritic mitochondria. (B) Percentage of mitochondria with protrusions. (C-E) Mushroom body neurons. Examples show mitochondrial protrusions (red arrowheads) in different shapes and sizes. Black arrowheads indicate a vesicle next to but not a part of the mitochondrion. The voxel of the FIB-SEM is 4x4x4 nm. (F) A mitochondrion from a protocerebral bridge neuron shows multiple protrusions (red arrowheads). The number on the micrograph indicates its z-position in the SEM image stack. Scale bars, 100 nm.

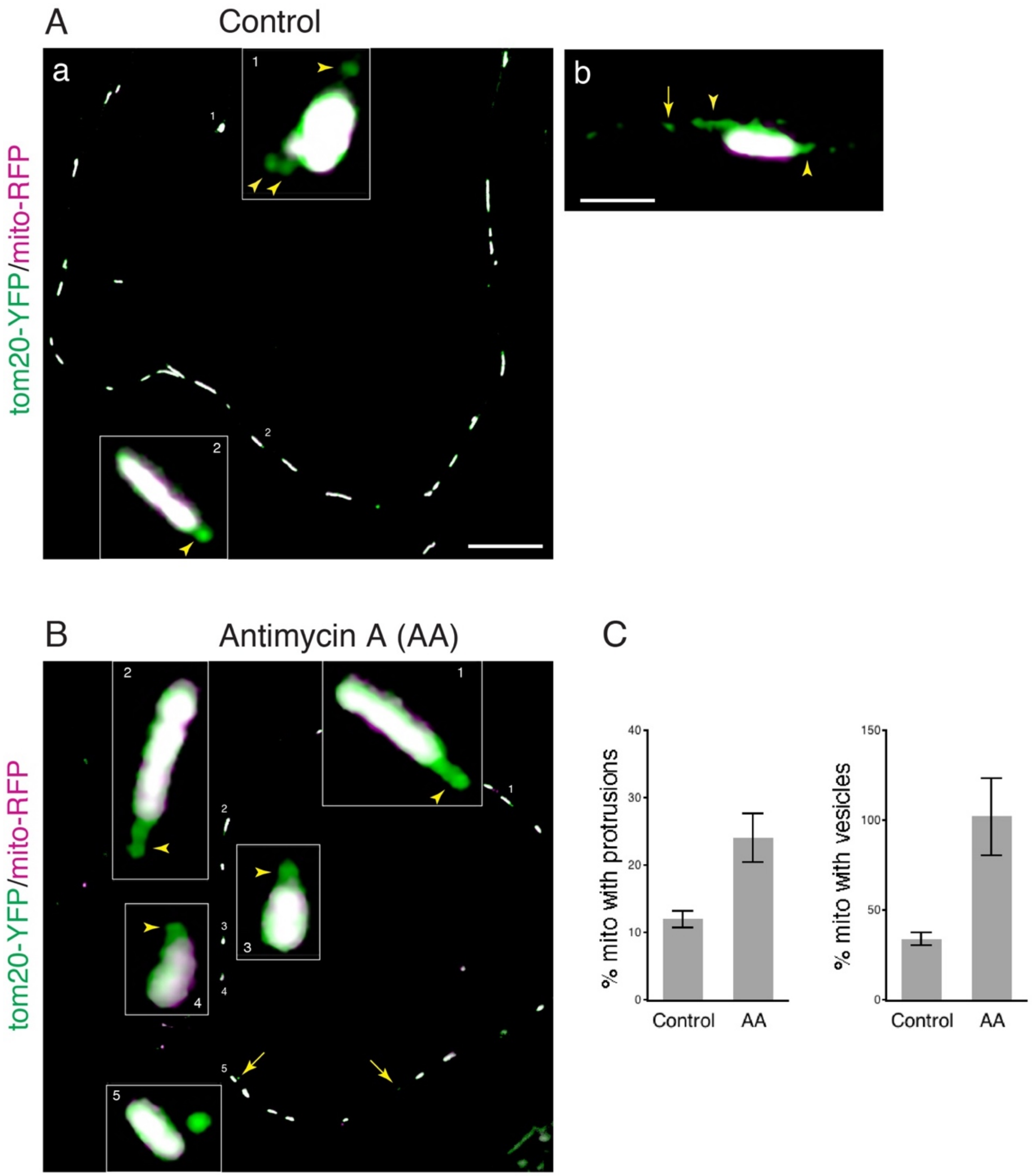

Figure S6. Fluorescence images of cultured hippocampal neurons expressing tom20-YFP and mito-RFP, Related to Figure 6. Boxed areas show enlarged views of tom20-YFP-illuminated mitochondrial protrusions (arrowheads) or vesicles (arrows). (A) untreated control; (B) AA-treated. (C) Percent of mitochondria with protrusions or vesicles (related to Figure 6H and Figure 6I, in which data are presented as number of mitochondrial protrusions or vesicles per mitochondrion). Data are represented as mean ± SEM. Student's *t* test was used for calculating the p values. $p < 0.01$ for analyses of both protrusions and vesicles. Scale bars in Aa and B, 10 mm; in Ab, 1 mm.

Transparent Methods

Animals

Adult male Sprague-Dawley rats were used for conventional transmission electron microscopy. Timed pregnant female Sprague-Dawley rats were used as the source of embryonic brain tissues for establishing cultures of hippocampal neurons. Planaria (*Dugesia tigrina*) were obtained from Carolina Biological Supplies. All animal procedures were approved by the NIA and NIDCD Animal Care and Use Committees and complied with the NIH Guide for Care and Use of Laboratory Animals. Animals used for producing the 3D EM datasets were described in the respective studies published previously (see below).

Reagents

DNA construct tom20-YFP was kindly provided by Dr. Chad Williamson (NICHD, NIH) and mito-RFP was kindly provided by Dr. Carolyn Ott (HHMI at Janelia Research Campus). Culture media and reagents including Neurobasal medium and B27 were from Invitrogen. Calcium phosphate mammalian transfection kit was from Clontech (#631312). Antimycin A (#A8674) and poly-L-lysine (#P2636) were from Sigma.

Transmission electron microscopy (TEM)

Sections of the rat hippocampi were prepared exactly as described in several of our previous studies (Petralia and Wenthold, 1999; Petralia et al., 1999; Petralia et al., 2010; Petralia et al., 2018). Briefly, rats were anesthetized and immediately transcardially perfused with 4% paraformaldehyde plus 0.5% glutaraldehyde. The brains were removed and post-fixed in the same fixative solution for 2 hours, and were vibratomed at 350 μm. The hippocampi were dissected from the brain sections, and were cryoprotected, frozen in a Leica EM CPC, and then embedded in Lowicryl in a Leica AFS freeze-substitution instrument. After staining with uranyl acetate and lead citrate, thin sections (from 3 rats) were examined in a JEOL JEM-2100 TEM microscope.

The planarian brains were prepared with the same procedure described above and used in previous studies (Petralia et al., 2015; Petralia et al., 2016). For the present study, new thin sections from the brains of 2 planaria were stained with uranyl acetate and lead citrate and examined in a JEOL JEM-2100 TEM microscope.

In both the rat hippocampus and planaria brains, definitive axons were identified by the presence of clusters of synaptic vesicles and/or a synapse; dendrites were identified by the presence of a synapse or characteristics of large dendrites, including a combination of tapering, even shape, microtubules, and multiple mitochondria and other organelles, as described (Petralia et al., 2010, Petralia et al., 2018). In the hippocampus, thin processes with the structural appearance of axons or thin dendrites, but without visible synapses, were defined as neurites. Also, in the hippocampus, large and irregular shaped processes with loose bundles of intermediate (i.e., glial filaments) were identified as glia processes.

FIB-SEM and ATUM-SEM datasets and analysis
The nucleus accumbens FIB-SEM dataset was produced in previous studies (Wu et al., 2017; Xu et al., 2017). The nucleus accumbens tissue was from an adult mouse (C57/BL6J). The mouse was transcardially perfused with a mixture of 2% glutaraldehyde and 2% depolymerized paraformaldehyde in 0.1 M phosphate buffer. The brain was removed and post-fixed in the same mixture overnight at 4°C, and 50-μm sections were prepared. Following additional processing as detailed in Wu et al. (2017) and Xu et al. (2017), FIB-SEM of the nucleus accumbens was produced. The FIB-SEM dataset used in the present study has 562 serial EM images with a voxel of 4x4x4 nm.

The somatosensory cortex ATUM-SEM (automatic tape-collecting ultramicrotome-scanning electron microscopy) dataset was produced in a previous study (Kasthuri et al., 2015). The somatosensory cortex tissue (layer V or V/VI) was from an adult mouse (BALB/c). The mouse was transcardially perfused with 200 ml (~ 5 ml/min flow rate) of fixative solution containing 2% glutaraldehyde, 4% paraformaldehyde and 0.2 mM $CaCl_2$ in cacodylate buffer (0.1M, pH 7.4). The brain was removed and post-fixed in the same fixative solution overnight at 4°C. The somatosensory cortex was then dissected, sectioned, and processed as described in detail in Kasthuri et al. (2015). The ATUM-SEM dataset of the somatosensory cortex consisted of 1850 serial EM images with a voxel of 6x6x30 nm.

The *Drosophilia* FIB-SEM of protocerebral bridge was produced as described previously (Takemura et al., 2017; Xu et al., 2017). Brain tissue was from a 5-day-old adult female CantonS G1xw1118 Drosophila. Vibratome brain slices (200 μm) were fixed in 2.5% glutaraldehyde and 2.5% paraformaldehyde in 0.1 M cacodylate for 10-15 min before processing for freeze-substitution, followed by embedding in Durcupan resin. Smaller vertical posts were then trimmed to the region of interest – protocerebral bridge – guided by X-ray tomography data obtained by a Zeiss Versa XRM-510 and optical inspection under a microtome. Details of the FIB-SEM production were described in detail previously (Xu et al., 2017).

We used VAST (Volume Annotation and Segmentation Tool)(Berger et al., 2018; Kasthuri et al., 2015) to visualize and annotate mitochondria in the brain SEM datasets. We examined mitochondria in axons and dendrites of neurons. Axonal mitochondria were identified as mitochondria in the synaptic vesicle-containing presynaptic terminals or in structures that can be traced to presynaptic terminals. Dendritic mitochondria were defined as mitochondria either in postsynaptic structures that directly form synaptic contact with presynaptic terminals, or in a dendrite, a part of which can be traced to form a synapse. Synapses of mouse neurons were identified based on the presence of synaptic vesicles, a synaptic cleft, and a clearly visible postsynaptic density (Figure S2E,F). Synapses of *Drosophila* protocerebral bridge neurons were identified based on the presence of synaptic vesicles, presynaptic T-bar, and postsynaptic density (i.e., Figure 5).

For assessing the number of mitochondria protrusions, we randomly selected mitochondria from axons or dendrites, and examined the mitochondria in their entirety in z-dimensions. For the mouse nucleus accumbens FIB-SEM dataset, a total of 58 axonal mitochondria and 42 dendritic mitochondria were examined. For the mouse somatosensory cortex ATUM-SEM dataset, 400 axonal mitochondria and 200 dendritic mitochondria were examined. For the *Drosophilia* FIB-SEM of protocerebral bridge dataset, 20 axonal mitochondria and 20 dendritic mitochondria were examined. For measuring the size of mitochondria in the *Drosophilia* protocerebral bridge neurons, we segmented the mitochondria in their entirety using VAST, then calculated the volume of the segmented mitochondria using MatLab (Berger et al., 2018). For 3D reconstruction of mitochondria, we used VAST followed by 3ds Max (Autodesk).

Neuron culture and transfection

Cultures of hippocampal neurons were prepared from embryonic day 18 rat brains using a described protocol (Kaech and Banker, 2006; Yao et al., 2015; Yao et al., 2017). Dissociated neurons were seeded at a density of ~200 cells/mm^2 on poly-L-lysine (1 mg/ml)-coated glass coverslips (no. 1.5) and grown in Neurobasal medium supplemented with B27. After growing in culture for 6 to 7 days (days in vitro), the neurons were transfected with tom20-YFP and mito-RFP using a calcium phosphate-based kit following the manufacturer's protocol (Clontech, #631312). Twenty-four hours after transfection, the neurons were incubated with 5 nM Antimycin A for 5 hours, followed by recovery in medium without Antimycin A for 1 hour. The neurons were immediately fixed in pre-warmed 4% paraformaldehyde and 4% sucrose for 15 minutes, and then washed gently, mounted in Prolong Gold antifade reagent, and stored at 4^{0}C before imaging. The experiments were repeated 5 times in 5 different batches of hippocampal neuronal cultures.

Fluorescence microscopy and analysis

Neurons expressing tom20-YFP and mito-RFP were examined, and images were acquired with an Apochromat 63x/1.4 numerical aperture objective lens on a Zeiss LSM 880 microscope with Airyscan (Carl Zeiss). All images were acquired at a 1024 x 1024-pixel resolution (1 pixel = 43.5 μm). In the present study, we focused on examining mitochondria in neurites in both control and experimental group. For each experiment, 10 images (67.8 μm^2 per image) from 2 coverslips were acquired. The image acquisition settings were kept the same between different experiments. The brightness, contrast, and levels of the images were adjusted evenly across the image for each channel in Adobe Photoshop and compiled in Adobe Illustrator. No additional digital image processing was performed.

Mitochondrial protrusions were visualized in Photoshop (after using the Auto Tone once) and defined with the following criteria: (1) protruding from - but still connecting to - mitochondria; (2) tom20-YFP positive; (3) mito-RFP negative - confirmed by the absence of RFP signal in individual RGB channels. The number of these mitochondrial protrusions were counted manually. Mitochondrial vesicles were defined as tom20-YFP positive puncta that were not connected to mitochondria. The number of these mitochondrial vesicles were counted using the Analyze Particles in imageJ with the particle size set at 5-100 pixel units. The number of mitochondria, which coexpress tom20-YFP and mito-RFP, were also counted using the Analyze Particles in image J with the particle size set at 100-infinity pixel units.

Statistical Analysis

Statistical analysis was performed using KaleidaGraph and Graphpad Prism. For comparison of two groups (Figure 6H-K; Figure S5A; Figure S6C), statistical significance was determined by two-tailed Student's *t* test. To determine the correlation (Figure 5I), Pearson's correlation analysis was used. Data are represented as mean ± SEM. The number of experimental replicates can be found in the figure legends. A p-value of < 0.05 was considered as a threshold for statistical significance. All p values are listed on the figures.

Transparent Methods References

Berger, D.R., Seung, H.S. and Lichtman, J.W. (2018). VAST (Volume Annotation and Segmentation Tool): Efficient Manual and Semi-Automatic Labeling of Large 3D Image Stacks. Front Neural Circuits. 12, 88

Kaech, S. and Banker, G. (2006). Culturing hippocampal neurons. Nat Protoc. 1, 2406-2415.

Kasthuri, N., Hayworth, K.J., Berger, D.R., Schalek, R.L., Conchello, J.A., Knowles-Barley, S., Lee, D., Vázquez-Reina, A., Kaynig, V., Jones, T.R., Roberts, M., Morgan, J.L., Tapia, J.C., Seung, H.S,. Roncal, W.G., Vogelstein, J.T., Burns, R., Sussman, D.L., Priebe, C.E., Pfister, H. and Lichtman, J.W. (2015). Saturated Reconstruction of a Volume of Neocortex. Cell. 162, 648-661.

Petralia, R.S. and Wenthold, R.J. (1999). Immunocytochemistry of NMDA receptors.Methods Mol Biol. 128, 73-92.

Petralia, R.S., Esteban, J..A, Wang, Y.X., Partridge, J.G., Zhao, H.M., Wenthold, R.J. and Malinow, R. (1999). Selective acquisition of AMPA receptors at hippocampus CA1 synapses during postnatal development. Nature Neurosci. 2, 31-36.

Petralia, R.S., Wang, Y.X., Hua, F., Yi, Z., Zhou, A., Ge, L., Stephenson, F.A. and Wenthold, R.J. (2010). Organization of NMDA receptors at extrasynaptic locations. Neuroscience. 167, 68-87.

Petralia, R.S., Wang, Y.X., Mattson, M.P. and Yao PJ. (2018). Invaginating Structures in Mammalian Synapses. Front Synaptic Neurosci. 10, 4.

Petralia, R.S., Wang, Y.X., Mattson, M.P. and Yao, P.J. (2015). Structure, Distribution, and Function of Neuronal/Synaptic Spinules and Related Invaginating Projections.

Neuromolecular Med. 17, 211-240.

Petralia, R.S., Wang, Y.X., Mattson, M.P. and Yao ,P.J. (2016). The Diversity of Spine Synapses in Animals. Neuromolecular Med. 18, 497-539.

Wu, Y., Whiteus, C., Xu, C.S., Hayworth ,K.J., Weinberg, R.J., Hess, H.F. and De Camilli, P. (2017). Contacts between the endoplasmic reticulum and other membranes in neurons. Proc Natl Acad Sci. 114, E4859-E4867.

Xu, C.S., Hayworth, K.J., Lu, Z., Grob, P., Hassan, A.M., García-Cerdán, J.G., Niyogi, K.K., Nogales, E., Weinberg, R.J. and Hess, H.F. (2017). Enhanced FIB-SEM systems for large-volume 3D imaging. Elife. 6, e25916.

Yao, P.J., Manor, U., Petralia, R.S., Brose, R.D., Wu, R.T., Ott, C., Wangm Y.X., Charnoff, A., Lippincott-Schwartz, J. and Mattson, M.P. (2017). Sonic hedgehog pathway activation increases mitochondrial abundance and activity in hippocampal neurons. Mol Biol Cell 28, 387-395

Yao, P.J., Petralia, R.S., Ott, C., Wang, Y.X., Lippincott-Schwartz, J. and Mattson, M.P. (2015). Dendrosomatic Sonic Hedgehog Signaling in Hippocampal Neurons Regulates Axon Elongation. J Neurosci. 35, 16126-16141